Research Article

Chi-Young Jung and Jong-Han Lee*

Crack closure and flexural tensile capacity with SMA fibers randomly embedded on tensile side of mortar beams

https://doi.org/10.1515/ntrev-2020-0026
received January 8, 2020; accepted January 29, 2020

Abstract: In this study, an experimental investigation was conducted to assess the flexural tensile strength and crack-closing performance of mortar beams containing short shape memory alloy (SMA) fibers, randomly distributed only on the tensile side. The SMA fibers were mainly composed of titanium (Ti), nickel (Ni), and niobium (Nb). In addition, the effect of tensile steel wires on the flexural strength and crack-closing performance was evaluated. A four-point bending test was performed to evaluate the post-cracking tensile strength. This study also suggested a proper model to calculate the ultimate flexural moment of the SMA fiber–embedded beams. Subsequently, a heating plate that could be installed at the bottom of the beam was used to induce the shape memory effect and measure the closed crack width. This study assessed the crack-closing performance induced by the SMA fibers at the bottom side of the beams and the resistance of the tensile wires in the beams.

Keywords: shape memory alloy, shape memory effect, crack closure, ultimate flexural strength, residual flexural strength, volume fraction, fiber reinforced, cement mortar beams

1 Introduction

Shape memory alloys (SMAs) are considered smart materials with two distinctive properties: superelasticity and shape memory effect (SME). Superelasticity refers to the ability to return to a predefined shape upon unloading after undergoing large nonlinear deformation. In other words, inelastic deformation, which occurs above the austenite finish temperature A_f, can be recovered promptly when the applied load is removed. SME is the phenomenon of the alloy returning to its initial shape. This implies that inelastic deformation remains upon unloading but is recovered upon heating the alloy to a temperature above A_f.

SMAs have been mainly used in the field of medical, aerospace, and automotive engineering since their development in the 1960s [1,2]. In recent years, the application of SMAs has been extended to the field of architectural and civil engineering. Particularly in bridges and buildings, it is necessary to control oscillations caused by external forces, such as winds, earthquakes, and traffic, which could induce progressive damage and failure [3–5]. Therefore, SMAs in the form of a wire and plate have been used to provide resistance to external loads and control the behavior of the structural members. Dolce and Cardone [6,7] performed cyclic torsion and tensile tests to examine the secant stiffness, energy loss, equivalent damping, and residual strain of the NiTi SMA wires. The results of the study showed that the SMA wires had high potential for use as a seismic device with considerable energy dissipation capacity and fatigue resistance. Mekki and Auricchio [8] introduced an energy dissipation device for cables in cable-stayed bridges using superelasticity and damping capability of SMAs. They assessed the effects of the area, length, and location of the SMA device on the control of the displacement of the cables. Torra et al. [9] also investigated the performance of the SMA wire dampers in stayed cables and provided suggestions on the appropriate length and required number of SMA wires. Zhang and Zhu [10] proposed SMA wire dampers for controlling the seismic response of a three-story building. A NiTi SMA wire was used in the proposed SMA dampers for large energy dissipation during earthquakes. In addition to dampers, deformation control devices, such as braces, connections, and base isolators,

* **Corresponding author: Jong-Han Lee,** Department of Civil Engineering, Inha University, Incheon 22212, Republic of Korea, e-mail: jh.lee@inha.ac.kr
Chi-Young Jung: Seismic Simulation Test Center, Pusan National University, Yangsan 50612, Republic of Korea

have been proposed for enhancing the seismic performance of structures [11–14].

Studies have been conducted on the prestressing or strengthening of the structural and concrete members [15–17]. Abdulridha and Palermo [18] conducted an experimental study to assess the performance of an SMA steel–reinforced concrete slender shear wall, which showed considerable displacement restoration after being subjected to large drifts. Branco et al. [19] strengthened a composite wall using the hysteretic behavior of NiTi wires, which proved to be a promising technique in reinforcing old building walls. Shahverdi et al. [20] used the SME of the iron-based SMA strips, which develops from recovery stress owing to their mechanical fixation, for strengthening reinforced concrete structures. Mas et al. [21] proposed the use of NiTi SMA cables for longitudinal reinforcement in concrete beams on the basis of uniaxial tensile and cyclic tests. They showed a limiting factor of SMA cables with low modulus of elasticity in applications but observed that SMA cables showed good strain recovery owing to the superelastic property. Choi et al. [22] attempted to induce recovery stress of SMA wires in reinforced concrete beams by using the heat of hydration of the concrete.

SMA wires or bars have a concern of being connected at both ends and interfering with steel bars in concrete structures. Recently, several studies have employed an idea of fiber-reinforced cement composites, prepared by mixing discontinuous short-length fibers with cementitious materials for field applications [23–30]. Lee et al. [31] measured crack widths in mortar beams owing to SME of the SMA fibers installed between cracks. This experimental study showed that the closed crack width increased as the number of fibers increased. Furthermore, Lee et al. [32] distributed NiTi and NiTiNb fibers randomly in mortar beams and evaluated the crack-closing performance and the residual flexural capacity of the SMA fiber–reinforced mortar beams. Pazhanivel et al. [33] investigated the effects of NiTi SMA short fibers on the mechanical and flexural properties of the glass fiber–reinforced polymer composites. Xu et al. [34] proposed a finite element modeling of the pseudoelasticity and SME in the SMA fiber–reinforced composites using a representative volume element and a commercial software platform.

Applications of SMAs are still limited because of a lack of understanding of material properties, insufficient knowledge of SMA-based design, and high cost [14,35]. This study was aimed at improving the functionality and usability of SMAs in cement-based members. Beam specimens with a length of 160 mm and a cross section of 40 × 40 mm were designed. SMA fibers were randomly mixed with cementitious materials. Subsequently, the SMA fiber–reinforced cement composites were distributed only at the bottom of the beams, where the beams are most vulnerable to cracking. The SMA fibers mainly comprised titanium (Ti), nickel (Ni), and niobium (Nb). The austenite finish temperature was designed to be around 100°C to prevent damage to the cementitious material during the heating process. A four-point bending test was performed to evaluate the tensile flexural strength and cracks were generated at the bottom of the beam during the test. After that, a heating plate that could be installed at the bottom of the beam was used to induce the SME and measure the closed crack width. The effects of the SMA fibers on the crack-closing performance and flexural tensile strength of beams were determined for fiber volume fractions of 0.50%, 0.75%, and 1.00%.

2 Experiments

2.1 Preparation of specimens and material properties

In this study, beam specimens with a cross section of 40 × 40 mm and a length of 160 mm were designed. Figure 1 shows the dimensions and geometry of the

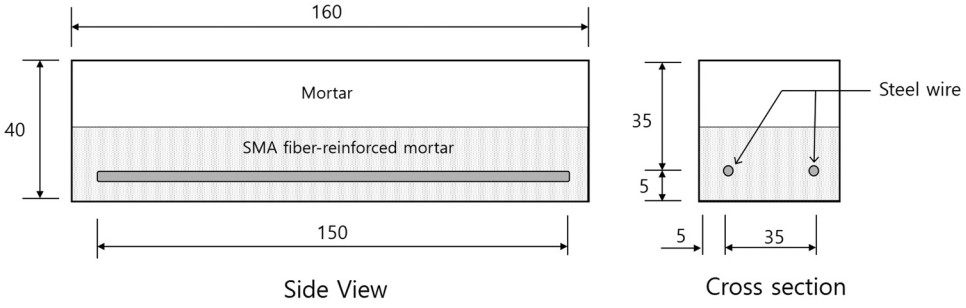

Figure 1: Geometry and cross section of a beam specimen (units: mm).

specimens, including a cross-sectional view. The SMA fibers with a length of 30 mm and a diameter of 0.67 mm were fabricated from NiTi and NiTiNb SMA wires with compositions of 56.8% Ni and 43.2% Ti, and 42.5% Ni, 45.3% Ti, and 12.2% Nb, respectively.

The water-to-cement and sand-to-cement ratios were 0.40 and 2.5, respectively. Superplasticizer was added at 1.0% by the cement mass. Therefore, the amounts of water, cement, and sand used in the study were 0.428, 1.07, and 2.14 kg, respectively. Cement and sand were mixed under dry conditions for approximately 3 min. After dry mixing, water was added to the mixture: two-thirds of water was first mixed for approximately 3 min, and the remaining water was mixed for 1 min. SMA fibers were then added to the mixture, and the cement composites randomly mixed with SMA fibers were prepared. The cement composites incorporated with SMA fibers were poured only in the bottom half of the beam, as shown in Figure 1. Smooth two steel wires with 2 mm in diameter were installed at 5 mm from the bottom of the beam specimen. Immediately after that, normal cement mortar was poured in the top half of the beam.

The test variable considered in this study was the volume fractions of the SMA fibers, 0.50%, 0.75%, and 1.00%. In addition, this study evaluated the effect of tensile steel bars on the flexural strength and crack-closing capacity. Table 1 lists the names and numbers of the specimens with test variables. The experimental data of the NiTi SMA specimens were taken from the previous study [36], which was designed by an author of the article.

Table 1: Specimen names and test variables

Specimen name	Types of SMA fiber	Types of tensile bar	Fiber volume fraction (%)
B000	None	None	None
B000-TB		Smooth wire	
B000-NiNb	NiTiNb	None	0.00
B050-NiNb			0.50
B075-NiNb			0.75
B100-NiNb			1.00
B000-NiNb-TB		Smooth wire	0.00
B050-NiNb-TB			0.50
B075-NiNb-TB			0.75
B100-NiNb-TB			1.00
B000-NiTi	NiTi	None	0.00
B050-NiTi			0.50
B075-NiTi			0.75
B100-NiTi			1.00
B000-NiTi-TB		Smooth wire	0.00
B050-NiTi-TB			0.50
B075-NiTi-TB			0.75
B100-NiTi-TB			1.00

The SME of the SMA results from a phase transformation from the martensitic to austenitic state. Austenite start and finish temperatures used in this study, A_s and A_f, were 74.2 and 100.3°C for the NiTi SMA fiber and 80.1 and 93.9°C for the NiTiNb SMA fiber. In fact, A_f was designed to prevent damage to the cementitious matrix during the heating process. In addition, the mechanical properties of the SMA fibers and steel bars – the yielding and ultimate stresses and the modulus of elasticity – were determined by conducting uniaxial tensile tests. Vision measurement and image analysis technique using targets on a wire were used to accurately obtain the stress–strain curves of the NiTi and NiTiNb SMA and the round steel wires, as shown in Figure 2. The yielding stress obtained by the 0.2% offset method was approximately 1,064 and 853 MPa for NiTi and NiTiNb SMA fibers, respectively. The ultimate stress of the NiTi and NiTiNb SMA fibers was approximately 1,467 and 1,133 MPa, respectively. The modulus of elasticity of the SMA fibers was 35.5 GPa, as presented in Figure 2. The smooth steel wire showed the yielding stress of approximately 328 MPa, ultimate strength of 422 MPa, and modulus of elasticity of 102.6 GPa.

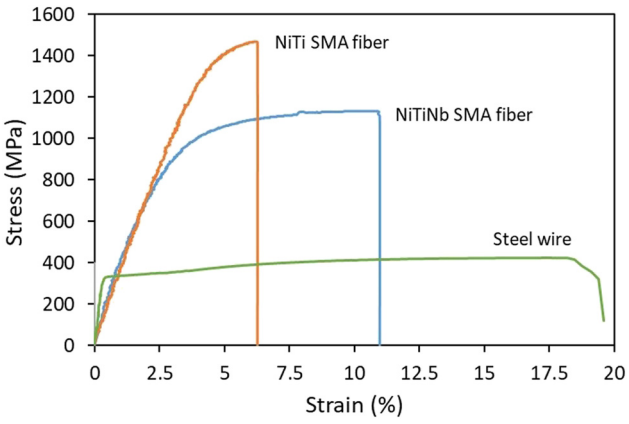

Figure 2: Stress and strain curves of the SMA fibers and steel wires.

2.2 Experimental setup and procedure

A four-point bending test was performed for evaluating the flexural strength of the beam reinforced with SMA fibers on the tensile bottom side. The beams developed permanent flexural cracks during the bending test. Therefore, heating was applied to the beams, and the extent to which cracks were closed by the SME of the SMA fibers was evaluated.

Figure 3 shows the setup and instrumentation for the bending tests and crack-closing tests. The beam span was set to 120 mm under simply supported conditions. The load was applied under displacement control at a rate of 0.1 mm/min. The distance between the loading points on the top surface of the beam was 300 mm, which led to a constant moment in the middle of the beam. The magnitude of the load was measured using a load cell mounted on an actuator, and the vertical deflection was simultaneously measured with a linear voltage displacement transducer (LVDT) installed in the middle of the beam, as shown in Figure 3a. A preliminary test found that the first cracking occurred at a vertical deflection of around 0.2 mm, and thus, the bending test was continued up to a vertical deflection three times the first cracking deflection, which is around 0.6 mm. However, the deflection of 0.6 mm was adjusted appropriately to prevent the collapse of the beam. Subsequently, the applied load was gradually removed to measure the widths of permanent cracks formed at the bottom of the beam.

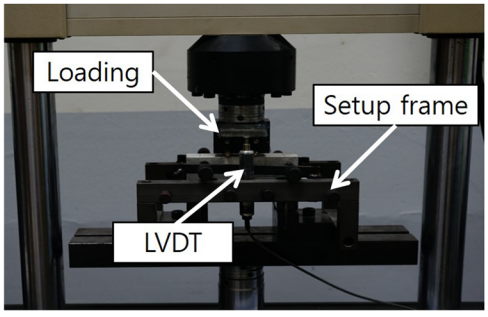

(a)

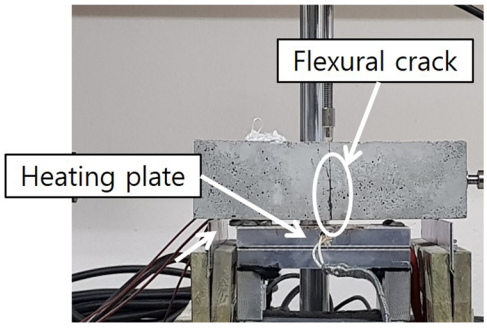

(b)

Figure 3: Experimental setup: (a) beam test and (b) crack-closing test.

To evaluate the flexural crack closing, heat was applied to activate the SME of the SMA fibers embedded in the beam. A heating plate that could be placed at the bottom of the beam was fabricated in this study, as shown in Figure 3b. The beam was heated up to 120°C by using a controller installed on the heating plate. Thermocouples were installed on the side surfaces at the middle of the beam to ensure that the temperature of all the SMA fibers in the beam approached the target temperature. After the target temperature was maintained for about 30 min, a magnifying lens was used to measure crack widths and compare the widths before and after heating. The crack width was also measured after the beam was cooled to room temperature to ensure that the closed crack width remained unchanged.

3 Results and discussion of bending tests

3.1 Load and deflection curves

Figure 4 shows an example of load and vertical deflection curves plotted from load cell and LVDT measurements for the control specimens and the NiTiNb SMA fiber–embedded beam specimens with fiber volume fractions (v_f) of 0.50%, 0.75%, and 1.00%. The load and vertical deflection curves of the beam specimens with NiTi SMA fibers, plotted in ref. [36], were similar. The load increases almost linearly with the deflection. The load, at which a crack was initiated on the beam, was defined as the cracking load P_{cr}. The control beam specimens without tensile wires showed a significant decrease in the load resistance and immediate flexural failure once a crack occurred and propagated, as shown in Figure 4a. On the other hand, the beam specimens without tensile wires but incorporated with SMA fibers on the tensile bottom side of the beam showed a load resistance after a crack occurred. The load resistance dropped immediately after a crack occurred on the beam but recovered to maintain some residual resistance until failure, as shown in Figure 4b–d. In particular, as the volume fraction of the SMA fibers increased, the post-cracking load resistance tended to increase. The beams with tensile wires showed a typical behavior resisted by wires, particularly after crack, as expected. Table 2 summarizes the critical and ultimate loads, P_{cr} and P_u, obtained from the beam tests.

The trends in P_{cr} and P_u were evaluated with changes in the fiber volume fraction and tensile wire for the NiTiNb and NiTi SMA fibers, as presented in Figure 5. The mean value of P_{cr} ranged from 3.85 to 5.30 kN for the NiTiNb fiber–embedded beams and from 3.85 to 4.83 kN for the NiTi SMA fiber–embedded beams with fiber volume fractions of 0 to 1.00%. The linear regression analysis showed that the increase of P_{cr} was approximately 1 kN when SMA fibers were incorporated in the beams. Therefore, the influence of SMA fibers on P_{cr} was minimal, and no significant difference was found between the control beams and the SMA

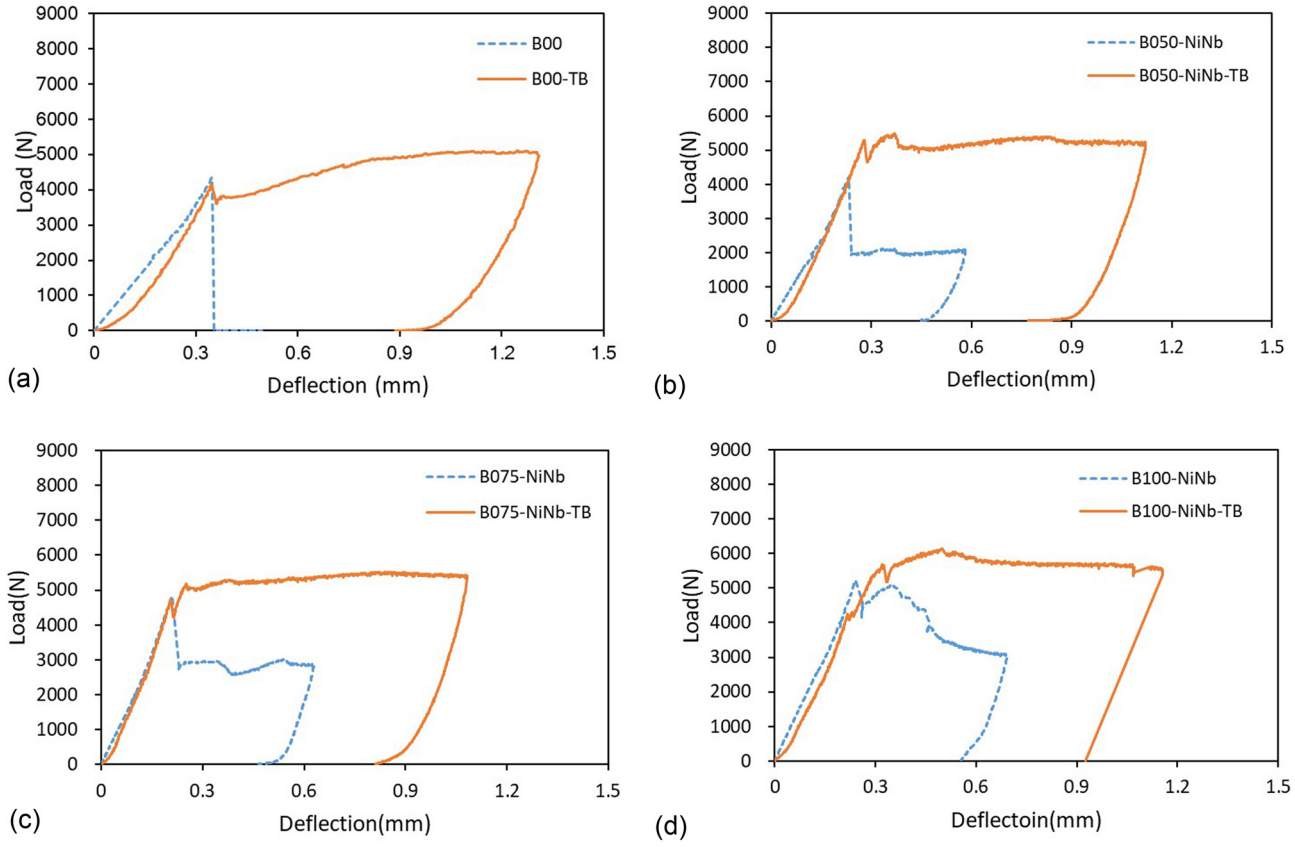

Figure 4: Example of load and deflection curves of the beam specimens with and without tensile wires: (a) v_f = 0%, (b) v_f = 0.50%, (c) v_f = 0.75%, and (d) v_f = 1.00%.

fiber–embedded beams, as well as the embedment of tensile wires. P_u also tended to increase somewhat with increasing fiber volume fraction. According to the linear regression analysis, P_u increased by approximately 1.7 and 0.72 kN per a 1% increase of the NiTiNb and NiTi SMA fibers, respectively, as shown in Figure 6. The little higher P_u in the NiTi fiber–embedded beams is attributed to the higher ultimate strength of the NiTi fiber.

3.2 Ultimate flexural moment

This study assessed the ultimate flexural moment of the SMA fiber–embedded beams with tensile wires. Figure 7 shows the simplified stress distribution with a linear strain distribution. Based on the simplified rectangular stress distribution in the compression and tension zones, the ultimate moment can be calculated as follows:

$$M_u = f_t\left(\frac{bh}{2}\right)d_1 + A_s f_y d_2, \quad (1)$$

where A_s and f_y are the area and yielding stress of the tensile wire, respectively; b and h are the width and depth of the cross section, respectively; and f_t is the ultimate tensile stress of the SMA fiber–embedded cement composites. According to American concrete institute (ACI) 544.4R-88 [37], based on the study of Henager and Doherty [38], f_t is calculated by the following equation:

$$f_t = 0.0072\left(\frac{l}{d_f}\right)v_f \alpha_b, \quad (2)$$

where l and d_f are the length and diameter of the fibers, respectively, and α_b is the bond efficiency factor, which was taken as 1 for straight fibers in the study. f_t can also be calculated using the following equation [39].

$$f_t = \alpha_o \sigma_f v_f \alpha_b, \quad (3)$$

where σ_f is the ultimate strength of the fibers and α_o is the orientation factor, which was taken as 0.64 for the beams with fibers only incorporated in the tension zone [40]. A main difference is that equation (3) accounts for the stress of the fibers instead of the aspect ratio of geometry.

Table 2: Summary of the test results for the beam specimens with and without tensile wires

Specimens	P_{cr} (kN)	P_u^{exp} (kN)	M_u^{exp} (kN mm)	Specimens	P_{cr} (kN)	P_u^{exp} (kN)	M_u^{exp} (kN mm)
B000-1	4.01	4.01	80.1	B000-TB-1	3.67	5.40	108.1
B000-2	4.01	4.01	80.1	B000-TB-2	4.26	5.27	105.4
B000-3	3.60	3.60	72.1	B000-TB-3	4.30	5.09	101.9
B000-4	3.80	3.80	75.9	B000-TB-4	3.86	5.12	102.3
Average	3.85	3.85	77.1	Average	4.02	5.22	104.4
(Std error mean)	(0.097)	(0.097)	(1.94)	(Std error mean)	(0.154)	(0.072)	(1.45)
B050-NiNb-1	4.31	4.31	86.3	B050-NiNb-TB-1	4.51	5.31	106.2
B050-NiNb-2	5.72	5.72	114.4	B050-NiNb-TB-2	4.24	5.06	101.1
B050-NiNb-3	4.17	4.17	83.4	B050-NiNb-TB-3	5.30	5.48	109.6
Average	4.74	4.74	94.7	Average	4.68	5.28	105.6
(Std error mean)	(0.494)	(0.494)	(9.88)	(Std error mean)	(0.309)	(0.123)	(2.47)
B075-NiNb-1	4.81	4.81	96.3	B075-NiNb-TB-1	4.70	5.29	105.9
B075-NiNb-2	5.71	5.71	114.1	B075-NiNb-TB-2	4.30	5.59	111.9
B075-NiNb-3	4.97	4.97	99.4				
Average	5.16	5.16	103.3	Average	4.50	5.44	108.9
(Std error mean)	(0.274)	(0.274)	(5.49)	(Std error mean)	(0.204)	(0.150)	(2.99)
B100-NiNb-1	5.22	5.22	104.5	B100-NiNb-TB-1	4.25	6.01	120.3
B100-NiNb-2	4.11	4.11	82.1	B100-NiNb-TB-2	4.27	6.28	125.6
B100-NiNb-3	4.51	4.51	90.2				
Average	4.61	4.61	92.3	Average	4.26	6.15	122.9
(Std error mean)	(0.327)	(0.327)	(6.54)	(Std error mean)	(0.011)	(0.132)	(2.64)
B050-NiTi-1	4.02	4.02	80.4	B050-NiTi-TB-1	3.93	5.26	105.3
B050-NiTi-2	4.08	4.08	81.6	B050-NiTi-TB-2	3.76	5.39	107.8
B050-NiTi-3	3.77	3.77	75.4	B050-NiTi-TB-3	3.90	5.00	100.1
B050-NiTi-4	3.17	3.17	63.4	B050-NiTi-TB-4	3.71	5.35	106.9
Average	3.96	3.96	75.2	Average	3.82	5.25	105.0
(Std error mean)	(0.208)	(0.208)	(4.15)	(Std error mean)	(0.054)	(0.086)	(1.72)
B075-NiTi-1	4.26	4.26	85.3	B075-NiTi-TB-1	4.53	6.42	128.4
B075-NiTi-2	4.24	4.24	84.9	B075-NiTi-TB-2	4.35	6.65	132.9
B075-NiTi-3	4.87	4.87	97.4	B075-NiTi-TB-3	4.30	6.70	134.0
B075-NiTi-4	4.33	4.33	86.5	B075-NiTi-TB-4	4.20	6.28	125.7
Average	4.43	4.43	88.5	Average	4.34	6.51	130.2
(Std error mean)	(0.149)	(0.149)	(2.99)	(Std error mean)	(0.069)	(0.098)	(1.95)
B100-NiTi-1[a]	2.49	2.49	49.9	B100-NiTi-TB-1	4.23	6.47	129.5
B100-NiTi-2	5.70	5.70	114.0	B100-NiTi-TB-2	6.20	6.87	137.4
B100-NiTi-3	4.93	4.93	98.6	B100-NiTi-TB-3	4.54	6.43	128.7
B100-NiTi-4	4.39	4.39	87.8	B100-NiTi-TB-4	4.34	7.24	144.9
Average	5.01	5.01	100.1	Average	4.83	6.76	135.1
(Std error mean)	(0.380)	(0.380)	(7.60)	(Std error mean)	(0.461)	(0.190)	(3.81)

[a]These values do not include the calculation of average and standard deviation.

Table 3 compares the mean ultimate flexural moments obtained from the bending tests with those from equations (2) and (3). The ratio of the ultimate moment obtained using equation (2), M_u^{ACI}, to the experimental value, M_u^{exp}, was 0.58 to 0.70. This is similar to the previous discussion by Swamy and Al-Taan [40], who showed the calculated-to-test flexural moment of 0.772, indicating the underestimation of the ultimate flexural moment using the ACI model [37]. On the other hand, the ultimate flexural moment calculated using equation (3), $M_u^{[39]}$, was overestimated by approximately 141–191%. As a result, equation (2), which accounts for the geometry aspect ratio of the fibers, tends to underestimate the ultimate moment of the fiber-reinforced cement composite. On the contrary, equation (3) overestimates the ultimate moment because of an unclear estimation of the strength of the fibers at the ultimate state.

When calculating the ultimate flexural moment of the SMA fiber–embedded beams with tensile wires, this study suggests that the ultimate strain of the fibers was assumed to be four times the yielding strain of the tensile wire.

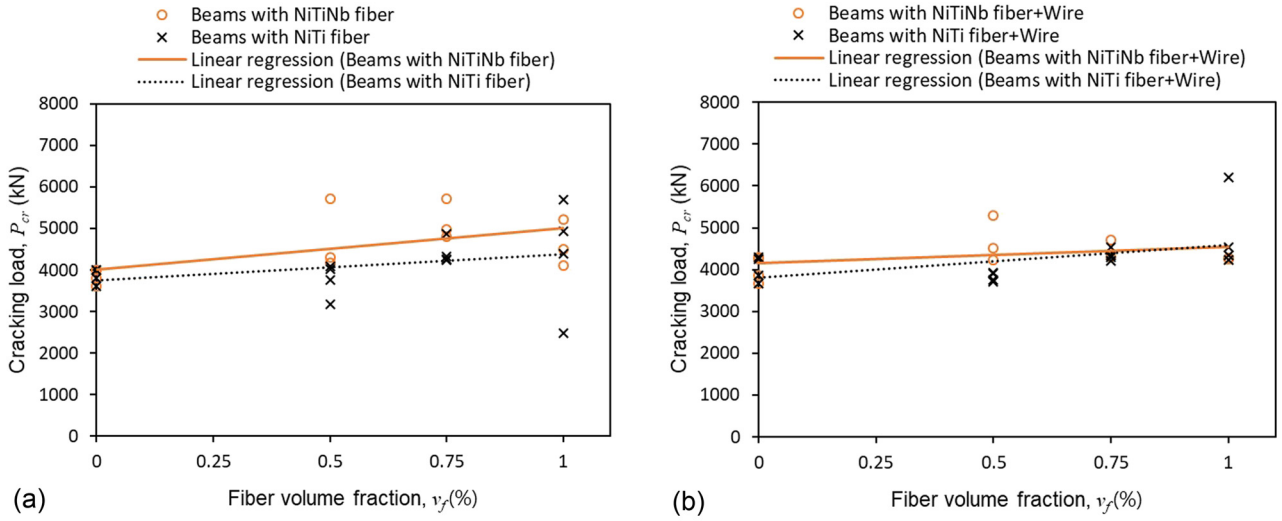

Figure 5: Cracking loads of the beam specimens with fiber volume fractions: (a) beam specimens without tensile wires and (b) beam specimens with tensile wires.

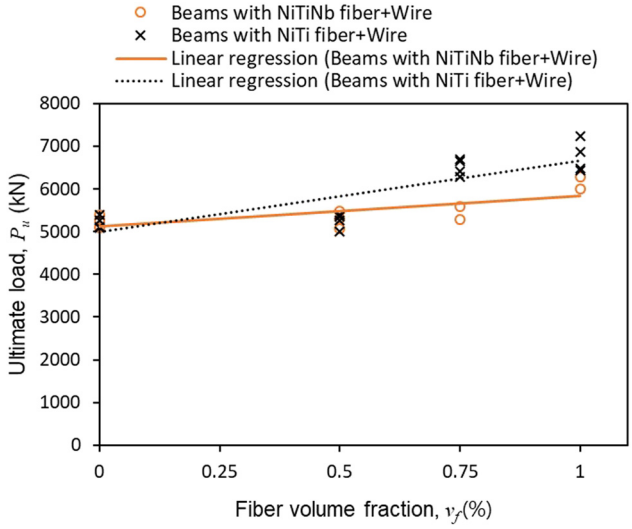

Figure 6: Ultimate loads of the beam specimens with fiber volume fractions.

The ultimate moment calculated using the proposed method, M_u^{rev}, was reasonably in agreement with the experimental value. The ratio of M_u^{rev} to M_u^{exp} ranged from 0.89 to 1.06.

3.3 Residual flexural tensile strength

From the load and deflection relationships obtained from the bending tests, the residual tensile strengths of the beams embedded with NiTiNb SMA fibers were investigated. The NiTi SMA fiber–embedded beams, which showed relatively large slip in the beginning of the bending tests [36], were excluded in this investigation. The flexural tensile strength is calculated by the following equation [41]:

$$f = \frac{PL}{bd^2}, \tag{4}$$

where P is the applied load and b, d, and L are the width, depth, and span length of the beam specimen, respectively. The cracking strength, denoted by f_{cr}, is the strength at the first cracking load P_{cr}. The mean vertical deflection at P_{cr} was calculated to be 0.26 mm. Therefore, the residual strengths after cracking, denoted by f_{400} and f_{300}, were defined at deflections of $L/400$ (= 0.3 mm) and $L/300$ (= 0.4 mm), respectively. f_{400} represents the reduction in the flexural strength immediately after cracking, and f_{300}, at which cracks are propagated to the top of the cross section and the beam is close to collapse, represents the trend in the residual strength with an increase in the post-cracking deflection.

Figure 8 shows the cracking and residual strengths with fiber volume fractions from 0 to 1.00%. The dotted lines were obtained from a linear regression analysis. The cracking strength f_{cr} increases with the fiber volume fraction, as shown in Figure 8a, but the increase rate in f_{cr} is relatively small. According to the linear regression, f_{cr} increased by approximately 1.40 MPa for a 1.00% increase in the SMA fiber volume fraction. The residual flexural strengths f_{400} and f_{300} showed a definite increase in the SMA fiber–embedded beams with increasing fiber volume fraction, as shown in Figure 8b and c. The dotted lines for f_{400} and f_{300} show a rate of increase of approximately 7.00 and 6.49 MPa for a 1.00% increase in the fiber volume

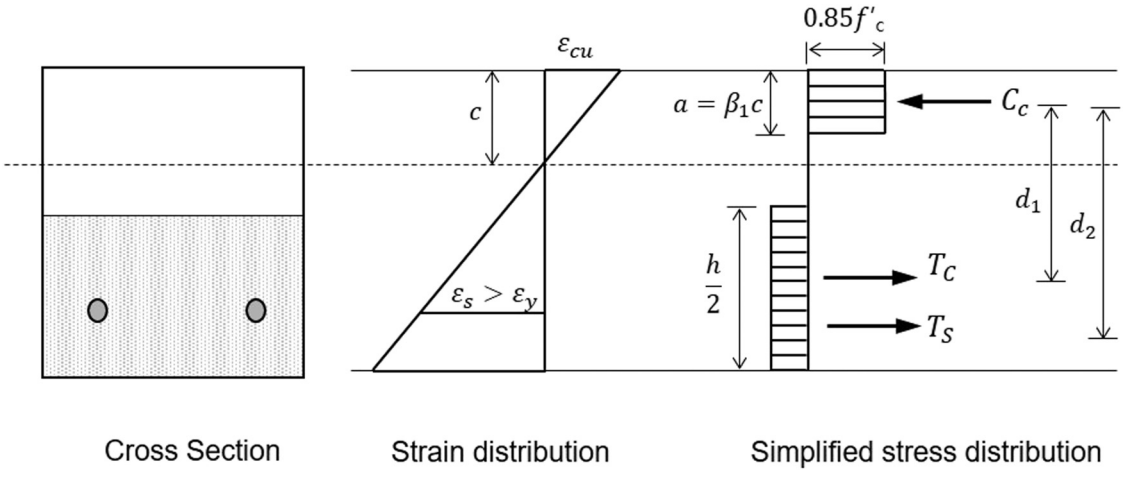

Figure 7: Strain and stress distributions of the SMA fiber–embedded beam with tensile wires at the ultimate state.

Table 3: Comparisons of the mean ultimate flexural moment of the SMA fiber–embedded beams with tensile wires

Specimen name	M_u^{exp} (kN mm)	M_u^{ACI} (kN mm)	$\frac{M_u^{ACI}}{M_u^{exp\,I}}$	$M_u^{[39]}$ (kN mm)	$\frac{M_u^{[39]}}{M_u^{exp\,I}}$	M_u^{rev} (kN mm)	$\frac{M_u^{rev}}{M_u^{exp\,I}}$
B050-NiNb-TB	105.6	73.9	0.70	148.7	1.41	101.0	0.96
B075-NiNb-TB	108.9	75.8	0.70	184.9	1.70	115.7	1.06
B100-NiNb-TB	122.9	77.7	0.63	219.4	1.79	130.2	1.06
B050-NiTi-TB	105.0	73.9	0.70	170.1	1.62	100.9	0.96
B075-NiTi-TB	130.2	75.8	0.58	215.2	1.65	115.6	0.89
B100-NiTi-TB	135.1	77.7	0.58	257.4	1.91	130.1	0.96

fraction, respectively. For the control specimens without SMA fibers, which proceed to collapse immediately after cracking, f_{400} and f_{300} are zero. The mean f_{400} and f_{300} ranged from 2.82 to 6.68 MPa and from 2.62 to 6.33 MPa, respectively, in the beams with the volume fraction of SMA fibers from 0.50 to 1.00%. In particular, f_{300} was approximately 87% to 95% of f_{400}, indicating that the amount of the decrease in the residual flexural strength is small and that the post-cracking residual strength is maintained in the SMA fiber–embedded beams.

3.4 Energy absorption capacity

This study also evaluated the energy absorption capacity of the NiTiNb SMA fiber–embedded beams. The energy absorption capacity can be calculated using the load and deflection values up to a certain point, that is, the areas below the load and deflection curves. Figure 9 shows the energy absorption capacities calculated up to the cracking deflection, $L/400$, and $L/300$, which are denoted by E_{cr}, E_{400}, and E_{300}, respectively. The linear regression line, dotted line in Figure 9a, exhibits an almost constant slope in the range of fiber volume fractions of 0 to 1.00%. This indicates that the effect of SMA fibers on E_{cr} is negligible, which corresponds to a small increase in the cracking strength with an increase in the fiber volume fraction. On the other hand, E_{400} and E_{300} show a large increase with an increase in the fiber volume fraction from 0 to 1.00%, as shown in Figure 9b and c. As the fiber volume fraction increased from 0.50 to 1.00%, the mean E_{400} up to $L/300$ increased from 0.579 to 0.767 J, and E_{300} increased from 0.726 to 1.114 J. According to a linear regression analysis of the fiber volume fraction ranging from 0 to 1.00%, E_{400} and E_{300} showed an increase of 0.768 and 1.170 J, respectively.

4 Results and discussion of crack-closing tests

The bending tests resulted in crack initiation at the bottom of the beam, and the cracks propagated to the top of the beam section. After the applied load was

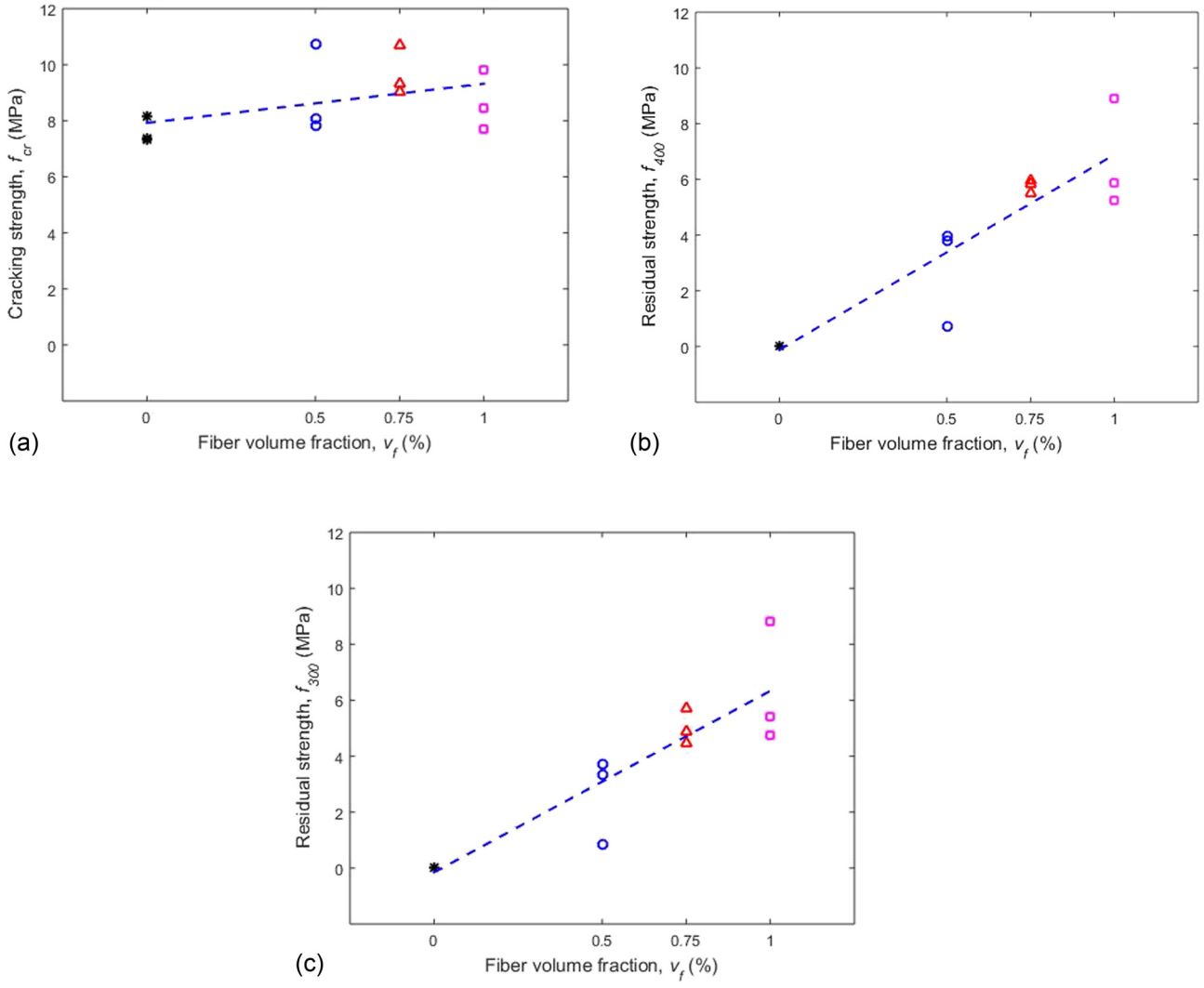

Figure 8: Residual flexural strengths of the beam specimens with fiber volume fractions: (a) f_{cr}, (b) f_{400}, and (c) f_{300}.

completely removed in a gradual manner, the width of the flexural crack was measured at the bottom of the beam. The crack width was measured using a magnifying lens at five locations along the crack. To close the crack, the SMA fibers embedded at the bottom of the beam were heated up to at least the austenite finish temperature by using the heating plate, as described in Section 2.2. The heating continued when a thermocouple attached to the beam surface in the middle of the beam reached the target temperature of 120°C. After the SME of the SMA fibers in the beam was fully activated, the crack width was measured again at the same locations used for the measurement before heating, as shown in Figure 10. The crack width was also measured after the SMA fiber–embedded beam was cooled to room temperature to confirm that the closed crack width was unchanged.

Figure 11 shows the crack widths measured before and after heating and the percentage of the crack closure for the NiTiNb and NiTi SMA fiber–embedded beams with and without tensile wires. For the beams without tensile wires, shown in Figure 11a, the NiTi SMA fiber–embedded beams show more rapid decrease in crack width, which indicates greater crack-closing performance, than the NiTiNb fiber–embedded beams. The closed crack widths ranged from 0.16 to 0.23 mm and from 0.27 to 0.34 mm for the NiTiNb and NiTi SMA fiber–embedded beams, respectively. The percentage of crack closure, defined as the ratio of the closed crack width to the initial crack width, was 34.7%, 37.2%, and 44.3% for the NiTiNb fiber–embedded beams and 56.4%, 65.4%, and 66.7% for the NiTi fiber–embedded beams with fiber volume fractions of 0.50%, 0.75%, 1.00%, respectively. The crack-closing performance of the NiTi

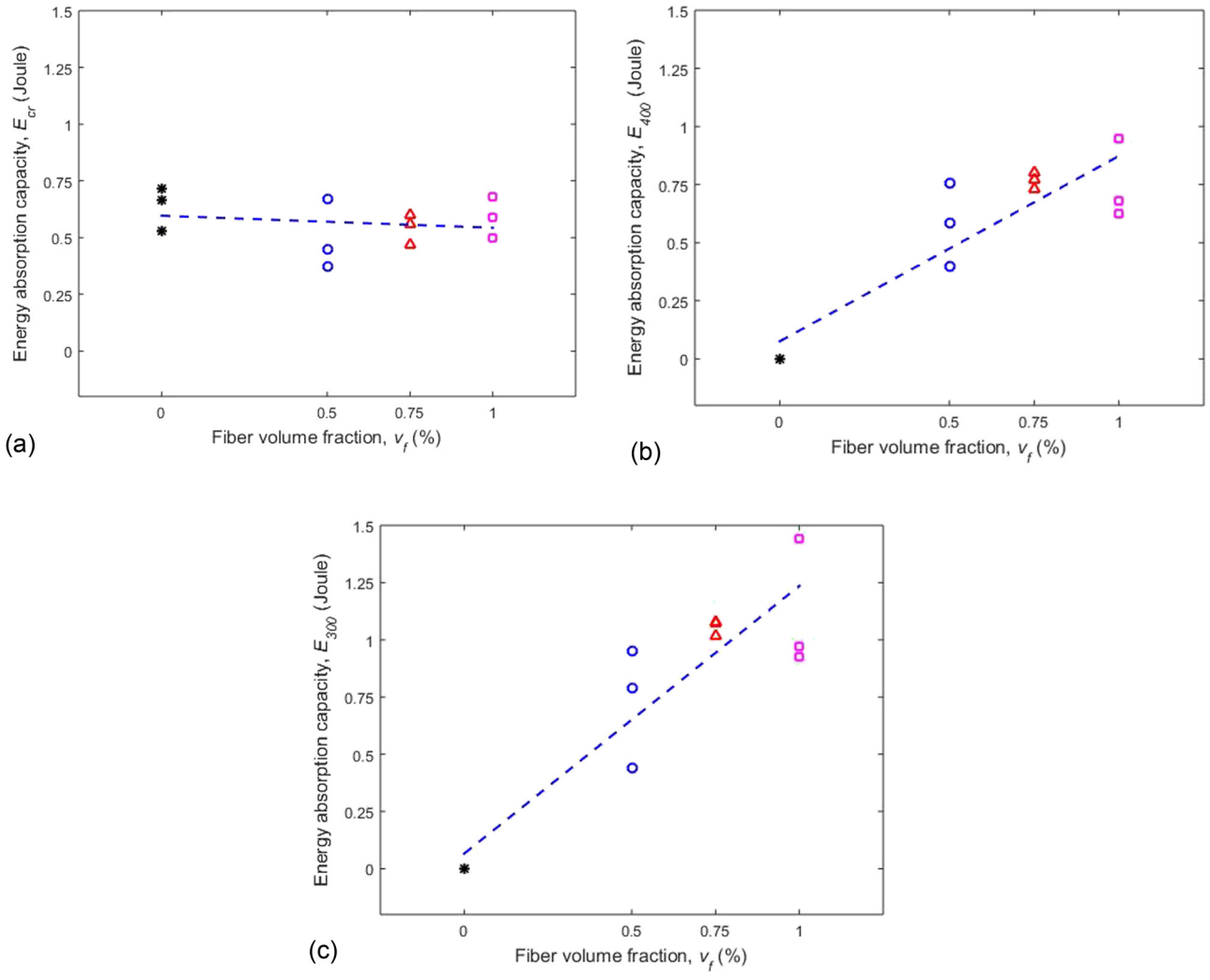

Figure 9: Energy absorption capacities of the beam specimens with fiber volume fractions: (a) E_{cr}, (b) E_{400}, and (c) E_{300}.

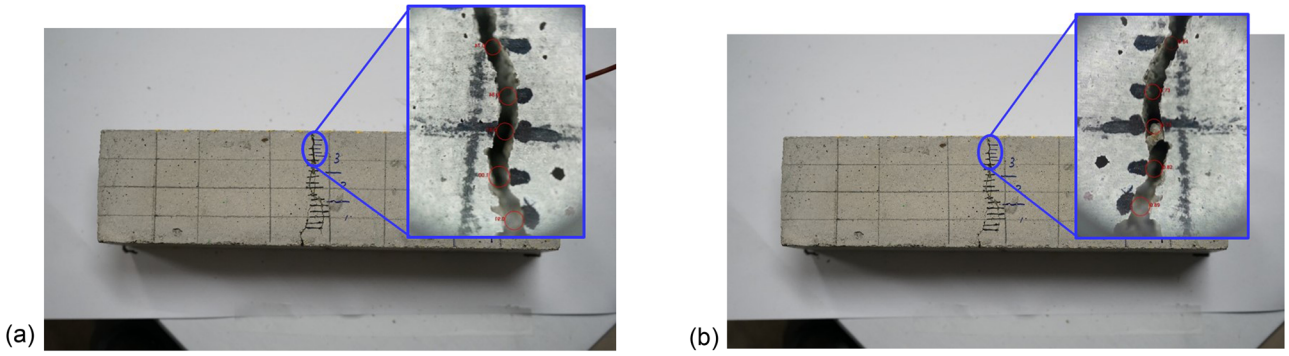

Figure 10: Examples of crack width measurements on the SMAF-075 specimen: (a) before and (b) after the activation of the SME in the SMA fibers.

SMA fiber–embedded beams increased by around 22–28% in the range of 0.50–1.00% fiber content on the tensile bottom side. In the case of the beam specimens with tensile wires, the crack-closing performance also tended to increase with increasing SMA fiber content on the tensile bottom side. However, the beams with tensile wires showed small and similar crack-closing performance regardless of the types of

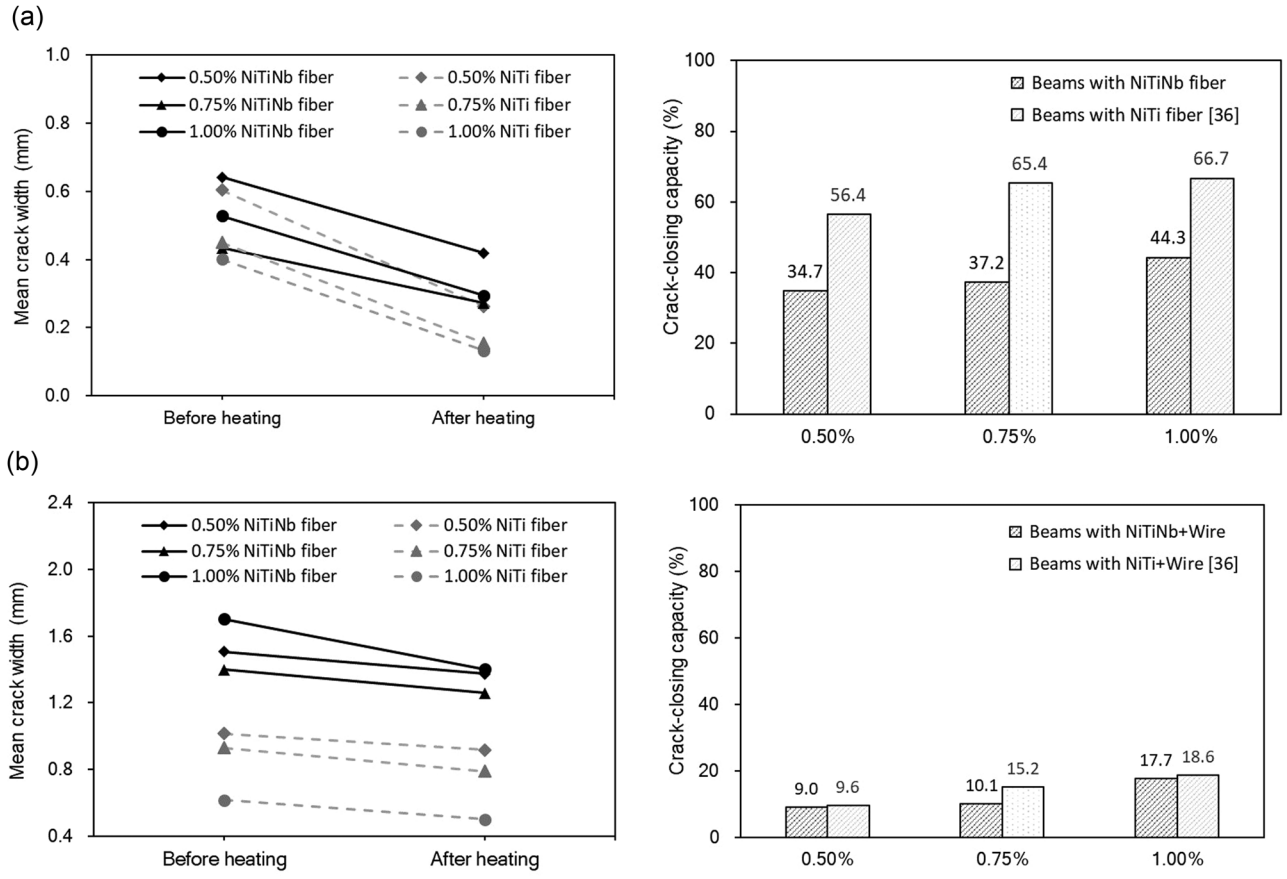

Figure 11: Crack closure from the SME in the SMA fibers with fiber volume fractions: (a) beam specimens without tensile wires and (b) beam specimens with tensile wires.

SMA fibers, as shown in Figure 11b. This is because of the resistance of the tensile wires, which reduces the crack-closing performance induced by the SME of the SMA fibers embedded in the beam.

5 Conclusions

This study proposes cement composites containing two types of SMA fibers randomly distributed in mortar. The cement composites were poured only in the bottom part of the beam specimens, which is most vulnerable to cracking. The SMA fiber–embedded cement composites can influence the flexural tensile strength of a beam and also provide crack-closing capability.

In the four-point bending tests, the control beams showed a rapid decrease in the load resistance and sudden brittle failure. The beams embedded with SMA fibers showed some load resistance after cracking. f_{300} was approximately 87–95% of f_{400}, which indicates that the post-cracking strength was maintained until failure. The energy capacities E_{400} and E_{300} also showed a large increase with an increase in the fiber volume fraction from 0 to 1.00%.

This study discussed some models of the ultimate flexural moment for the SMA fiber–embedded beams with tensile wires. Previous models largely differed from the experimental values. Therefore, this study suggested the ultimate strain of the fibers as four times the yielding strain of the tensile wires when calculating the ultimate flexural moment of the SMA fiber–embedded beams.

The bending tests generated permanent flexural cracks at the bottom of the beam. Heating was applied to activate the SME of the SMA fibers embedded on the bottom side of the beam to close the flexural cracks. The beam specimens with tensile wires tended to increase the crack-closing performance with increasing SMA fiber content on the tensile bottom side. However, the beams with tensile wires showed small and similar crack-closing performance regardless of the types of SMA fibers.

Acknowledgments: This research was supported by the Inha University Research Grant and a grant from the Basic

Science Research Program (NRF-2016R1D1A1B03935722) through the National Research Foundation (NRF) of Korea.

References

[1] Jani JM, Leary M, Subic A, Gibson MA. A review of shape memory alloy research: applications and opportunities. Mater Des. 2014;56:1078–113.

[2] Torra V, Martorell F, Lovey FC. Civil engineering applications: specific properties of NiTi thick wires and their damping capabilities. Shape Memory Superelast. 2017;3(4):403–13.

[3] Wang W, Fang C, Yang X, Chen Y, Ricles J, Sause R. Innovative use of a shape memory alloy ring spring system for self-centering connections. Eng Struct. 2017;153:503–15.

[4] Lu X, Zhang L, Li Y. Improvement to composite frame systems for seismic and progressive collapse resistance. Eng Struct. 2019;186:227–42.

[5] Li R, Ge H, Usami T, Shu G. A strain-based post-earthquake serviceability verification method for steel frame-typed bridge piers installed with seismic dampers. J Earthquake Eng. 2017;21(4):635–51.

[6] Dolce M, Cardone D. Mechanical behaviour of shape memory alloys for seismic applications 1. Martensite and austenite NiTi bars subjected to torsion. Int J Mech Sci. 2001;43:2631–56.

[7] Dolce M, Cardone D. Mechanical behaviour of shape memory alloys for seismic applications 2. Austenite NiTi wires subjected to tension. Int J Mech Sci. 2001;43:2657–77.

[8] Mekki OB, Auricchio F. Performance evaluation of shape-memory-alloy superelastic behavior to control a stay cable in cable-stayed bridges. Int J Non-Lin Mech. 2011;46(2):470–7.

[9] Torra V, Isalgue A, Auguet C, Carreras G, Lovey FC, Terriault P, et al. SMA in mitigation of extreme loads in civil engineering: damping actions in stayed cables. Appl Mech Mater. 2011;82:539–44.

[10] Zhang Y, Zhu S. Seismic response control of building structures with superelastic shape-memory alloy wire dampers. J Eng Mech. 2008;134(3):240–51.

[11] Dieng L, Helbert G, Chirani SA, Lecompte T, Pilvin P. Use of shape memory alloys damper device to mitigate vibration amplitudes of bridge cables. Eng Struct. 2013;56:1547–56.

[12] Massah SR, Dorvar H. Design and analysis of eccentrically braced steel frames with vertical links using shape memory alloys. Smart Mater Struct. 2014;23(11):115015.

[13] Yang CSW, Desroches R, Leon RT. Design and analysis of braced frames with shape memory alloy and energy-absorbing hybrid devices. Eng Struct. 2010;32(2):498–507.

[14] DesRoches R, Smith B. Shape memory alloys in seismic resistant design and retrofit: a critical review of their potential and limitations. J Earthquake Eng. 2004;8(3):415–29.

[15] Wang Z, Xu L, Sun X, Shi M, Liu J. Fatigue behavior of glass-fiber-reinforced epoxy composites embedded with shape memory alloy wires. Compos Struct. 2017;178:311–9.

[16] Gholampour A, Ozbakkaloglu T. Understanding the compressive behavior of shape memory alloy (SMA)-confined normal- and high-strength concrete. Compos Struct. 2018;202:943–53.

[17] Pareek S, Suzuki Y, Araki Y, Youssef MA, Meshaly M. Plastic hinge relocation in reinforced concrete beams using Cu–Al–Mn SMA bars. Eng Struct. 2018;175(15):765–75.

[18] Abdulridha A, Palermo D. Behaviour and modelling of hybrid SMA-steel reinforced concrete slender shear wall. Eng Struct. 2017;147:77–89.

[19] Branco M, Gonçalves A, Guerreiro L, Ferreira J. Cyclic behavior of composite timber-masonry wall in quasi-dynamic conditions reinforced with superelastic damper. Construct Build Mater. 2014;52:166–76.

[20] Shahverdi M, Michels J, Czaderski C, Motavalli M. Iron-based shape memory alloy strips for strengthening RC members: material behavior and characterization. Construct Build Mater. 2018;173:586–99.

[21] Mas B, Giggs D, Vieito I, Cladera A, Shaw J, Martínez-Abella F. Superelastic shape memory alloy cables for reinforced concrete applications. Construct Build Mater. 2017;148:307–20.

[22] Choi E, Hu JW, Lee JH, Cho B. Recovery stress of shape memory alloy wires induced by hydration heat of concrete in reinforced concrete beams. Eng Struct. 2015;26(1):29–37.

[23] Lee JH, Cho B, Choi E, Kim YH. Experimental study of the reinforcement effect of macro-type high strength polypropylene on the flexural capacity of concrete. Construct Build Mater. 2016;126:967–75.

[24] Liang H, Li S, Lu Y, Hu J, Liu Z. Electrochemical performance of corroded reinforced concrete columns strengthened with fiber reinforced polymer. Compos Struct. 2019;207:576–88.

[25] Lee JH, Hu JW, Kang JW. Effects of blades inside a nozzle on the fiber orientation and distribution in fiber-reinforced cement-based materials. Compos Struct. 2019;221:1–12.

[26] Wang JY, Gao XL, Yan JB. Developments and mechanical behaviors of steel fiber reinforced ultra-lightweight cement composite with different densities. Construct Build Mater. 2018;171:643–53.

[27] Lee JH, Cho B, Kim JB, Lee KJ, Jung CY. Shear capacity of cast-in headed anchors in steel fiber-reinforced concrete. Eng Struct. 2018;171:421–32.

[28] Zheng Q, Dong P, Li Z, Han X, Zhou C, An M, et al. Mechanical characterizations of braided composite stents made of helical polyethylene terephthalate strips and NiTi wires. Nanotechnol Rev. 2019;8(1):168–74.

[29] Gao Y, Jing H, Zhou Z. Fractal analysis of pore structures in graphene oxide–carbon nanotube based cementitious pastes under different ultrasonication. Nanotechnol Rev. 2019;8(1):107–15.

[30] Zhang P, Li Q, Wang J, Shi Y, Ling Y. Effect of PVA fiber on durability of cementitious composite containing nano-SiO_2. Nanotechnol Rev. 2019;8(1):116–27.

[31] Lee KJ, Lee JH, Jung CY, Choi E. Crack-closing performance of NiTi and NiTiNb fibers in cement mortar beams using shape memory effects. Compos Struct. 2018;202:710–8.

[32] Lee JH, Lee KJ, Choi E. Flexural capacity and crack-closing performance of NiTi and NiTiNb shape-memory alloy fibers randomly distributed in mortar beams. Composites Part B. 153:264–76.

[33] Pazhanivel K, Bhaskar GB, Elayaperumal A, Anandan P, Arunachalam S. Influence of Ni–Ti shape memory alloy short fibers on the flexural response of glass fiber reinforced polymeric compositeset. Appl Sci. 2019;1:789.

[34] Xu R, Bouby C, Zahrouni H, Zineb TB, Hu H, Potier-Ferry M. 3D modeling of shape memory alloy fiber reinforced composites by multiscale finite element method. Compos Struct. 2018;200:408–19.
[35] Jani JM, Leary M, Subic A. Designing shape memory alloy linear actuators: a review. J Intel Mater Syst Struct. 2017;28(13):1699–718.
[36] Kighuta K. Investigation of the flexual capacity and crack-closing effects in mortar beams reinforced with shape memory alloy fibers, Master thesis, Daegu Univeristy, 2018.
[37] ACI 544.4R-88. Design considerations for steel fiber reinforced concrete, American Concrete Institute. West Conshonocken; 1988 (reapproved 1999).
[38] Henager CH, Doherty TJ. Analysis of reinforced fibrous concrete beams. Proceedings ASCE; 1976, 12(ST-l). p. 177–88.
[39] Hameed R, Sellier A, Turatsinze A, Duprat F. Flexural behaviour of reinforced fibrous concrete beams: experiments and analytical modelling. Pakistan J Eng Appl Sci. 2013;13:19–28.
[40] Swamy RN, Al-Taan SA. Deformation and ultimate strength in flexure of reinforced concrete beams made with steel fiber concrete. ACI J. 1981;78–36:395–405.
[41] ASTM C 1609. Standard test method for flexural performance of fiber reinforced concrete. West Conshonocken: American Society of Testing Material; 2007.